

Modeling, Design and Validation of Magnetic Hysteresis Motors

Original

Modeling, Design and Validation of Magnetic Hysteresis Motors / Galluzzi, Renato; Amati, Nicola; Tonoli, Andrea. - In: IEEE TRANSACTIONS ON INDUSTRIAL ELECTRONICS. - ISSN 0278-0046. - (2020), pp. 1-1.
[10.1109/TIE.2019.2901652]

Availability:

This version is available at: 11583/2734575 since: 2019-06-03T11:26:32Z

Publisher:

IEEE

Published

DOI:10.1109/TIE.2019.2901652

Terms of use:

This article is made available under terms and conditions as specified in the corresponding bibliographic description in the repository

Publisher copyright

IEEE postprint/Author's Accepted Manuscript

©2020 IEEE. Personal use of this material is permitted. Permission from IEEE must be obtained for all other uses, in any current or future media, including reprinting/republishing this material for advertising or promotional purposes, creating new collecting works, for resale or lists, or reuse of any copyrighted component of this work in other works.

(Article begins on next page)

Modeling, Design and Validation of Magnetic Hysteresis Motors

Renato Galluzzi, Nicola Amati, and Andrea Tonoli

Abstract—The use of hysteresis motors nowadays is limited to few niche-focused applications. Nevertheless, their intrinsic features make them ideal for next-generation high-speed machinery. Hysteresis motors are highly nonlinear and their behavior is heavily influenced by the initial magnetization state of the rotor active part. As such, the exploitation of hysteresis machine technology requires a reliable method to assess the torque capability, both numerically and experimentally.

The present paper proposes a finite-element model for the design of hysteresis motors. In this tool, rotor hysteresis is described through the vector generalization of the Jiles-Atherton model. For validation purposes, a prototype is defined based on a specific application. The torque of this prototype is experimentally characterized for different electrical loadings and rotor speeds. Subsequently, this output is measured after rotor magnetization at different levels. It is demonstrated that the initial condition of the rotor active part can be exploited in synchronous conditions to improve the machine output torque.

Index Terms—finite element analysis, hysteresis motors, magnetic hysteresis, rotating machines.

I. INTRODUCTION

MAGNETIC hysteresis machines have a simple structure with a conventional multiphase stator winding and a solid or laminated rotor made of semi-hard magnetic material (SHMM). In literature, hysteresis machines are regarded as self-starting motors and able to produce uniform torque from standstill to synchronous speed, accelerate and synchronize high-inertia loads [1]. In addition, magnetic hysteresis can be exploited in controllable clutches and couplers [2].

When compared to other motor technologies, hysteresis machines present limited power densities and low power factors. Therefore, their diffusion among electric machinery is narrowed to very few applications where constant, low-ripple torque is required, such as gyroscopes, clocks, magnetic ribbons in recorders, self-bearing motors and other low-power precision equipment [1], [3], [4].

However, the increasing need of high-speed motors over the last few years settles a promising scenario for hysteresis machines. At high speeds, the following fundamental issues arise in rotating electric machinery:

- *Mechanical strength* is an important constraint because the maximum attainable peripheral speed of a rotor is

proportional to the tensile strength of its material. Technologies that exploit sintered permanent magnets (PM) or laminated configurations are hindered in this regard. Sleeves and other retaining elements can be adopted to partially overcome this drawback at the cost of reducing the efficiency of the machine.

- *Rotordynamics* is a key aspect during speed transitions, where the rotor might cross one or more critical speeds. Solid rotors are able to provide high stiffness, which eventually can help to push critical speeds beyond the operating range of the machine.
- *Thermal behavior* is a common problem in induction motors, where torque is produced by rotor eddy currents. Although PM synchronous motors are less prone to rotor overheating, their materials are constrained to rather restrictive maximum temperature limits due to the risk of demagnetization.

As denoted in recent research works [5], [6], the solid-rotor hysteresis motor is a promising solution that addresses all the aforementioned issues:

- Some SHMMs offer elevated *mechanical strength* to match high peripheral speeds while preserving their structural integrity.
- From the *rotordynamic* point of view, a solid rotor leads to considerably higher flexural stiffness and critical speeds. Smoothness and perfect mechanical isotropy limit the occurrence of rotordynamic instability problems even further.
- Hysteresis devices are less prone to rotor *overheating* than induction machines due to their synchronization feature. In addition, *Curie temperatures* of SHMMs are well above those of PMs.

These motivations push SHMM-based solutions towards their adoption in the context of high-speed machinery [6], [7].

Another interesting feature of hysteresis motors is their ability to improve their torque performance after the magnetization of the rotor with an impulsive electrical overexcitation. Although this potential behavior has been highlighted in previous works [8], its proper experimental characterization has not been carried out.

The modeling, design and control of hysteresis motors is a challenging task mainly due to the nonlinear nature of their behavior. Recent research works have devoted their efforts to providing new alternatives in this context.

A first type of approach regards the use of lumped-parameter models to reproduce the behavior of the machine

Manuscript received Month xx, 2xxx; revised Month xx, xxxx; accepted Month x, xxxx.

The authors are with the Department of Mechanical and Aerospace Engineering, Politecnico di Torino, 10129 Turin, Italy (e-mail: renato.galluzzi@polito.it).

[9]–[11]. In general, these tools are difficult to tune due to the amount of parameters and the nonlinear nature of the problem.

A following refinement step is to use magnetostatic finite element (FE) simulations to extract the first harmonic of the magnetomotive waveform at the surface of the rotor ring. This information is then used to calculate the rotor hysteresis losses with the aid of a material model and ultimately, the electromagnetic torque [12]–[14]. Although results following this method give a fair indication of the real machine behavior, they lack information on the harmonic content of the flux density waveforms. In many cases, high-order magnetic flux density harmonics severely detract from the overall performance of the hysteresis motor [15].

To reach an improved reproduction of the hysteresis phenomenon, fully-numerical approaches exploit FE analysis. Frequency-domain methods that rely on the complex permeability model [6] imply a low computational burden, but they struggle when heavy saturation is present. To overcome this issue, Nasiri-Zarandi and Mirsalim enhanced the complex permeability representation with an iteration-based method to account for saturation effects [16]. In contrast, time-domain approaches implement a material model on the rotor ring elements to find a time-stepping solution [6], [17]: they are able to reproduce nonlinear behavior and magnetic saturation at the cost of computational overhead. In this last category, Padilha *et al.* have demonstrated that the Jiles-Atherton vector model is sufficient to reproduce the performance of an hysteresis motor with isotropic Fe-Co 17% hard iron rotor [18].

In motion control, the definition of nonlinear strategies that account for magnetic hysteresis have allowed to estimate the rotor flux orientation. Zhou *et al.* have validated experimentally these methods to perform accurate position control in three hysteresis motor prototypes [19].

To contribute building a solid background on hysteresis motors, the present research is motivated by

- the rekindled interest in hysteresis motors due to the already outlined advantages;
- the necessity of numerical tools able to model their behavior and aid their design; and
- the need of investigating their performance and controllability through experimental tests.

From the numerical point of view, the paper proposes a tool for the design of hysteresis motors. The model outlined in Section II exploits a vector generalization of the Jiles-Atherton model to represent the anisotropic hysteretic behavior of the rotor material. In this context, this work aims to demonstrate the suitability of a time-domain representation to account for intrinsic nonlinearities of hysteresis motors. Furthermore, the importance of using a vector hysteresis model in rotating machinery is also highlighted. Following application-specific guidelines, a prototype is designed through the proposed tool. Afterwards, in Section III, the design is validated experimentally.

From the experimental point of view, this research offers the characterization of a prototype at different speeds and electrical loadings. At first, the testing procedure is followed to quantify the hysteresis torque. Then, the torque capability of the prototype is measured after an initial rotor magnetization at

different supply levels. This last step demonstrates a substantial improvement of the machine performance with respect to the torque obtained purely from magnetic hysteresis. The state of the art lacks a proper characterization of this last aspect, which can be crucial to improve the torque performance of hysteresis motors.

II. METHOD

A. Overview

Assume a hysteresis machine with a three-phase winding of p pole pairs supplied by a sinusoidal balanced input at frequency f_s . Its rotor consists of a SHMM ring of volume V_h . Then, the torque is ideally speed-independent and given by

$$T = \frac{p}{2\pi} E_h V_h, \quad (1)$$

provided that the rotor slip is non-zero, i.e. its mechanical frequency is constrained to

$$f_m < p f_s. \quad (2)$$

Note that (1) is directly proportional to the hysteresis energy density E_h of the rotor ring. In the scalar case, this term is given by the hysteresis loop area between a generic magnetic field component H_i and flux density B_i :

$$E_h = \oint B_i dH_i \quad (3)$$

However, in rotating machinery, the field is not constrained to a fixed axis: it rather assumes a continuously changing direction over time. This rotating nature motivates the use of a vector-based hysteresis model, as presented in the following.

B. Model

The finite element model that describes the behavior of the analyzed machine solves an electromagnetic problem formulation in terms of the magnetic vector potential \mathbf{A}

$$\mathbf{B} = \nabla \times \mathbf{A}, \quad (4)$$

$$\nabla \times \mathbf{H} = -\sigma \frac{\partial \mathbf{A}}{\partial t}, \quad (5)$$

where \mathbf{B} is the magnetic flux density vector, \mathbf{H} is the magnetic field vector and σ is the electrical conductivity. Given the studied frequency range, σ is assumed null for all domains, except for the SHMM solid rotor ring.

Slot domains are fed according to the spatial distribution of the windings by a three-phase external current density supply of amplitude J_s and frequency f_s :

$$\begin{cases} J_a = J_s \cos(2\pi f_s t) \\ J_b = J_s \cos(2\pi f_s t + 2\pi/3) \\ J_c = J_s \cos(2\pi f_s t + 4\pi/3) \end{cases} \quad (6)$$

Air and slot domains follow the magnetic constitutive relation

$$\mathbf{H} = \frac{1}{\mu_0} \mathbf{B}, \quad (7)$$

where $\mu_0 = 4\pi \cdot 10^{-7}$ H/m is the permeability of free space. In turn, the stator obeys a nonlinear relation to account for iron saturation:

$$\mathbf{H} = f_{\text{Fe}}(|\mathbf{B}|) \frac{\mathbf{B}}{|\mathbf{B}|} \quad (8)$$

The SHMM rotor ring behavior is described through the vector generalization of the Jiles-Atherton model proposed by Bergqvist [20] and extensively outlined by Bastos and Sadowski [21]. This representation calculates a magnetization vector \mathbf{M} by solving

$$\frac{d\mathbf{M}}{dt} = \mathbf{c} \frac{d\mathbf{M}_a}{dt} + (\mathbf{I} - \mathbf{c}) \frac{d\mathbf{M}_i}{dt}, \quad (9)$$

such that

$$\mathbf{H} = \frac{1}{\mu_0} \mathbf{B} - \mathbf{M}. \quad (10)$$

Equation (9) associates the anhysteretic and irreversible magnetization terms (\mathbf{M}_a and \mathbf{M}_i , respectively) through the reversibility tensor \mathbf{c} . For the i th vector component, the anhysteretic behavior is expressed with the Langevin function

$$M_{a,i} = M_{s,i} \left(\coth \left(\frac{|\mathbf{H}_e|}{a_i} \right) - \frac{a_i}{|\mathbf{H}_e|} \right) \frac{H_{e,i}}{|\mathbf{H}_e|}; \quad (11)$$

here, $M_{s,i}$ is the saturation magnetization and $a_{s,i}$ the Langevin slope for the i th component. The vector \mathbf{H}_e describes the effective magnetic field that depends on the interdomain coupling tensor α :

$$\mathbf{H}_e = \mathbf{H} + \alpha \mathbf{M} \quad (12)$$

Finally, the irreversible magnetization vector is expressed by the nonlinear function

$$\frac{d\mathbf{M}_i}{dt} = \left[(\mathbf{k}^{-1} \mathbf{c}^{-1} \mathbf{M}_r) \frac{d\mathbf{H}_e}{dt} \right]^+ \frac{\mathbf{k}^{-1} \mathbf{c}^{-1} \mathbf{M}_r}{|\mathbf{k}^{-1} \mathbf{c}^{-1} \mathbf{M}_r|}, \quad (13)$$

with \mathbf{k} being the pinning tensor and

$$\mathbf{M}_r = \mathbf{c} (\mathbf{c} - \mathbf{I})^{-1} (\mathbf{M} - \mathbf{M}_a) \quad (14)$$

the reversible magnetization vector.

With second-rank diagonal tensors \mathbf{M}_s , \mathbf{a} , \mathbf{c} , \mathbf{k} and α , Bergqvist's vector generalization of the Jiles-Atherton model is able to reproduce anisotropic magnetic behavior under alternating and rotating excitations. Although the rotational nature is handled intrinsically by the proposed formulation, it has demonstrated favorable results when compared to experimental data obtained with a rotational single sheet tester [21].

C. Design guidelines

The goal of the design method is to provide a machine geometry able to fulfill torque and envelope constraints. To this end, different machine configurations can be simulated through the outlined methodology and compared. The underlying assumptions for this analysis are the following:

- 1) The rotor active part is a ring made of SHMM. Unlike scalar models, the proposed numerical approach can handle both isotropic and anisotropic magnetic properties. The disposition of these properties in space is represented

using a two-dimension cylindrical coordinate system with radial (r) and tangential (ψ) main components.

- 2) The stator three-phase winding presents double layers and full pitch. Distributed windings are usually preferred to minimize field harmonics [23]. However, a full-pitch topology was adopted due to in-house manufacturing constraints.
- 3) The root-mean-square (RMS) current density $J_{w,rms}$ on the winding conductors is bounded for continuous operation or transient overload. This limitation is heavily dependent on the cooling system of the machine [22]. Based on our previous prototyping experiences, the attainable slot fill factor k_f is approximately 30%. Hence, the slot current density amplitude is calculated as

$$J_s = \sqrt{2} k_f J_{w,rms}. \quad (15)$$

- 4) The stator teeth are shoeless to facilitate manual coil winding.
- 5) The average magnetic flux density norm on the back iron and the teeth shall not reach saturation, even in overload condition.

The following metrics are evaluated to identify the most suitable configuration:

- *Electromagnetic torque.* It is priority of the design to optimize the torque capability of the machine. In a 2D FE model, the torque can be evaluated through the Maxwell stress tensor as a line integral along the air gap to enclose the rotor [24]:

$$T = \frac{l_a}{\mu_0} \oint_0^{2\pi} (R_{ro} + g/2)^2 B_r B_\psi d\psi \quad (16)$$

where l_a is the active length, R_{ro} the rotor outside diameter and g the air gap length.

- *Magnetic flux density fundamental harmonic amplitude.* This feature is important to quantify the size of the hysteresis loops activated in both the tangential and radial directions.
- *Magnetic flux density total harmonic distortion.* This metric parameter is calculated, for both $i = r$ and $i = \psi$, as

$$\text{THD}(B_i) = \frac{\sqrt{\sum_{j=2}^N B_{j,i}^2}}{B_{1,i}} \quad (17)$$

It gives an indication of the harmonic content of the flux density with respect to the fundamental harmonic.

In general, higher fundamental components of the magnetic flux density lead to larger hysteresis loops and hence, greater output torque. However, the presence of harmonic distortion in B_i severely detracts from the overall performance of hysteresis motors [15] due to the introduction of minor loops and consequent reduction of the effective hysteresis loop area. Hence, magnetic flux density harmonic distortion is also a relevant design metric.

D. Application

The aforementioned modeling approach and design guidelines are followed to develop an inner-rotor hysteresis motor

TABLE I
HYSTERESIS MOTOR DESIGN SPECIFICATIONS.

| Parameter | Value | Unit |
|-------------------------|-------|------|
| Maximum torque | 0.3 | N m |
| Maximum speed | 5000 | rpm |
| Active length | 30 | mm |
| Stator outside diameter | 100 | mm |
| Rotor outside diameter | 43 | mm |
| Rotor inside diameter | 34.4 | mm |
| Air gap length | 0.5 | mm |

TABLE II
FeCrCo 48/5 MANUFACTURER DATA.

| Property | Value | Unit |
|------------------------|-------------|-------------------|
| Remanent flux density | 1.32 – 1.45 | T |
| Coercivity | 48 – 53 | kA/m |
| Maximum energy product | 48 – 55 | kJ/m ³ |
| Curie temperature | 650 | °C |
| Electrical resistivity | 0.7 | μΩ m |

for a water pumping application within automotive engine cooling systems. The initial design specifications are listed in Table I.

The rotor active part is a solid ring of FeCrCo 48/5 alloy provided by YY Magnetics (China). Raw samples of this SHMM are heat-treated while applying a magnetic field orthogonal to the ring cross section. Magnetic flux lines will pass predominantly in the tangential direction [25]. As a result, this direction will exhibit an advantageous maximum energy product that can potentially reduce the final prototype envelope if exploited correctly by the design.

The material manufacturer data is reported in Table II. Unfortunately, this information cannot be used to accurately reproduce the hysteresis behavior of the material and thus, is insufficient to support the modeling and numerical validation tools discussed in this paper. To address this shortcoming, two samples were extracted from the material and characterized on their radial and tangential axes, respectively, using a vibrating sample magnetometer (VSM). The obtained major loops were used to identify the Jiles-Atherton parameters listed in Table III. For this purpose, we performed a least-square curve fit between the scalar model and the experimental data as a function of the five model parameters in Table III. This task was executed for the radial and tangential cases. The identification method is a particular case of the approach described by Kis and Iványi [26], where the criterion function is the squared absolute error sum of the magnetic field evaluated for the magnetic flux density values specified by the experiments.

VSM test data and fitting loops are compared in Fig. 1. It is observed that the anisotropy indeed favors the tangential direction. The proposed model is able to reproduce the experimental major loops with an enclosed area error of -0.33% for the radial component and -1.21% for the tangential one. Furthermore, the model is able to reproduce minor-loop

TABLE III
FeCrCo 48/5 JILES-ATHERTON MODEL PARAMETERS.

| Parameter | Symbol | Component | | Unit |
|-----------------------|----------|-------------------|-------------------|------|
| | | r | ψ | |
| Maximum magnetization | M_s | $1.84 \cdot 10^6$ | $2.02 \cdot 10^6$ | A/m |
| Langevin slope | a | $9.93 \cdot 10^4$ | $9.94 \cdot 10^4$ | A/m |
| Pinning | k | $1.41 \cdot 10^5$ | $5.16 \cdot 10^4$ | A/m |
| Reversibility | c | 0.69 | 0.2 | – |
| Interdomain coupling | α | 0.16 | 0.15 | – |

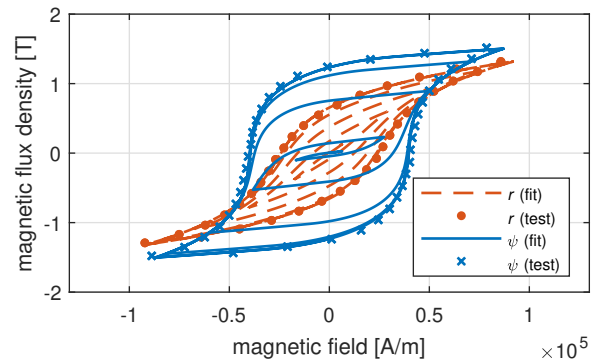


Fig. 1. FeCrCo 48/5 hysteresis loops. Experimental data for the radial (r) and tangential (ψ) components are compared to the Jiles-Atherton model fitting.

behavior. Although no experimental data are available to assess this aspect *a priori*, the validation of the hysteresis motor model through the output torque will indirectly confirm the goodness of the material model.

The obtained parameters can be used to populate the main diagonal of the model tensors. It is worth noting that the proposed representation relies on alternating tests in two orthogonal directions. More accurate representations can be obtained by characterizing hysteresis loops under rotational excitation [27].

For the purposes of this research, the described model was implemented in COMSOL Multiphysics as a time-stepping simulation. All the model equations, constitutive relations and constraints are natively supported features of COMSOL's Magnetic Fields interface from the AC/DC Module [28]. The Jiles-Atherton vector hysteresis model is also included: the user must only provide its tensor parameters.

To simplify the model and reduce the execution time, the rotor was locked in standstill position. This assumption is particularly valid for the hysteresis motor, where the torque is ideally speed-independent. In addition, only a pole pair of the machine was simulated with Dirichlet conditions on its side boundaries to impose even periodicity. The pole pair geometry was meshed with approximately 5600 triangular elements. A discretization with quadratic elements (Gauss points) was selected for all the domains. With this configuration, the models were simulated for $2p$ electrical cycles on a desktop PC with a Ryzen 5 1600 six-core processor running at 3.4 GHz and 16 GB of RAM. The average computational time was clocked slightly under 12 min.

TABLE IV
HYSTERESIS MOTOR DESIGN VARIANTS.

| Design | Slots | Pole pairs | Width [mm] | | Total slot area [cm ²] |
|--------|-------|------------|------------|-------|------------------------------------|
| | | | back iron | tooth | |
| A | 12 | 2 | 5.4 | 6.5 | 21.1 |
| B | 24 | 2 | 5.4 | 3.6 | 20 |
| C | 24 | 1 | 6.5 | 3.3 | 19.4 |
| D | 24 | 4 | 5 | 3.4 | 21.6 |

The design of the hysteresis motor is carried out considering the geometric constraints listed in Table I. Active length and stator outside diameter are fixed to account for the maximum envelope of the water pump. The rotor ring outside diameter is bounded by the application, while its inside diameter is selected to provide mechanical strength to the rotor structure. The air gap length is chosen to allow the radial clearance introduced by the plastic bushings that support the rotor shaft. Furthermore, the rotor architecture does not present a back iron layer. In this way, the flux path is forced to have a predominant component in the preferential (tangential) direction.

The design task is to provide a suitable stator configuration in terms of number of slots, pole pairs, stator back iron width and tooth width. To this end, several slot-pole pair combinations were tested following the outlined design method. For each case, the stator geometry was optimized with a coordinate search method to fulfill the magnetic flux density norm limit (1.2 T). In these calculations, the models were fed with a slot current density amplitude of 5 A/mm², which represents the maximum allowable overload considering a totally enclosed machine cooled by natural convection.

Among a wide variety of possible configurations, we report the four most promising ones in terms of output torque (Table IV). The simulation results for these design variants are illustrated in Fig. 2. To have a meaningful indication of the role of the fundamental harmonic and the total harmonic distortion, the rotor ring was subdivided into 100 layers in the radial direction. The radial and tangential magnetic flux density waveforms were extracted on each layer and the two aforementioned features were subsequently calculated. Finally, the results for all the layers were averaged to have a single numerical indicator for each feature. The output torque was also averaged in time after the machine startup transient.

The predisposition of the rotor as a ring without a back iron forces the field in the tangential direction. As a consequence, all the designs present a larger fundamental component and lower harmonic distortion in this direction. By converse, the radial contribution presents lower fundamental and higher distortion.

Designs C and D can be discarded from the final selection, as they present opposite limitations that hamper their output torque capability. Design C offers a very large fundamental harmonic amplitude for the tangential flux density at the cost of introducing the largest harmonic content in the radial direction. In contrast, design D offers very little harmonic distortion in all cases, but it fails in delivering a consistent hysteresis loop activation, as seen with its fundamental flux

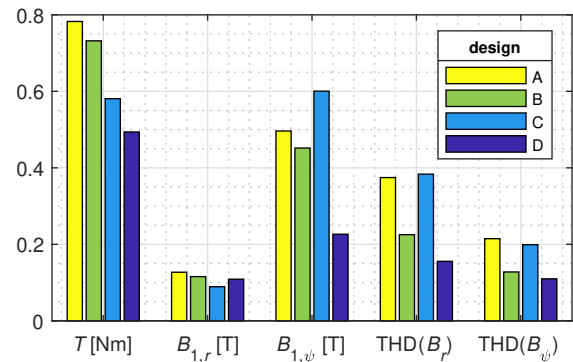


Fig. 2. Performance metrics for the four hysteresis motor design variants listed in Table IV: electromagnetic torque (T); radial and tangential magnetic flux density fundamental harmonic amplitude, rotor average ($B_{1,r}, B_{1,\psi}$); radial and tangential magnetic flux density total harmonic distortion, rotor average ($\text{THD}(B_r), \text{THD}(B_\psi)$).

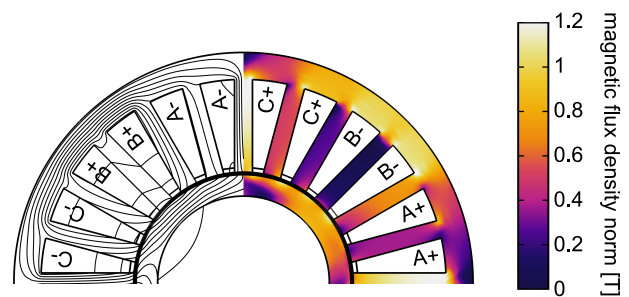


Fig. 3. Pole pair cross section of the final hysteresis motor design with magnetic flux density norm distribution (color map), winding layout (letters and signs) and magnetic vector potential z component (contours).

density components.

Among designs A and B, the former one offers slightly larger output torque (+50.7 mN m) and fundamental harmonic components (radial: +11.5 mT, tangential: +44.5 mT), but also significantly worse harmonic distortion than the latter option (radial: +0.15, tangential: +0.09). All in all, design B was preferred for the final prototype. This selection was driven by the fact that rotor losses in synchronous conditions are heavily influenced by high-order harmonics of the magnetic flux density and thus, design A is penalized in this regard.

Figure 3 illustrates the flux density norm color map and the contours of the magnetic vector potential z component for the design B topology. In this simulation, the rotor is locked and no eddy current losses are considered ($\sigma = 0$).

The torque output of this design can be calculated for two limit conditions:

- 1) $\sigma = 0$, the torque output does not depend on the supply frequency;
- 2) $\sigma = 1.43 \cdot 10^6$ S/m, $f_s = 166.7$ Hz \leftrightarrow 5000 rpm, a torque component due to rotor eddy currents is present.

The rotor ring position is locked in both cases. Numerical results in Fig. 4 demonstrate that the model captures the intrinsic nature of the hysteresis motor torque output: it follows a profile similar to the first magnetization curve of the SHMM. The machine is able to fulfill the maximum output torque requirement (0.3 N m) with a current density amplitude of

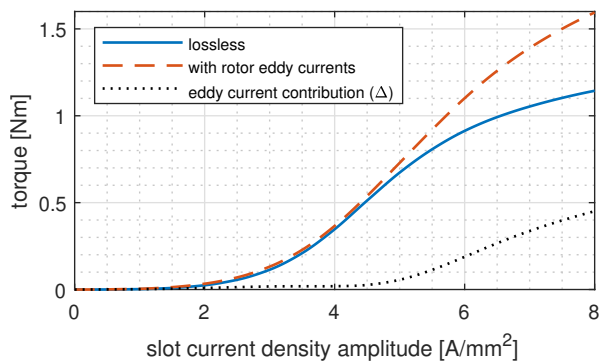


Fig. 4. Numerical model output torque as a function of the slot current density amplitude. The simulation is performed with a locked rotor position and a supply frequency of 166.7 Hz, both in the lossless condition and considering rotor eddy current losses. The difference (Δ) between these two conditions is also plotted.

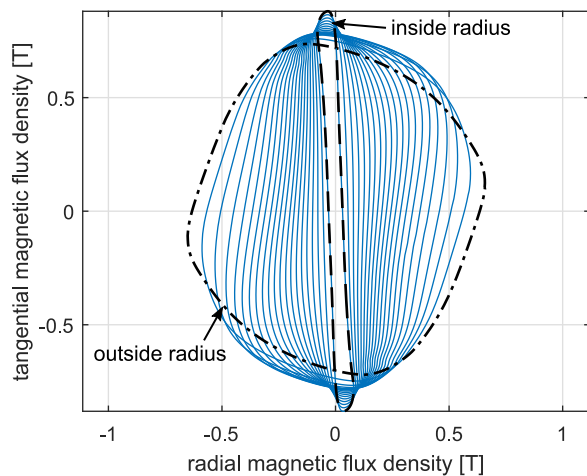


Fig. 5. Magnetic flux density locus for different rotor points along the radial coordinate. Increasing ellipticity of the locus is evident when going from the inside radius R_{ri} to the outside radius R_{ro} .

3.8 A/mm². In addition, rotor eddy currents have a strong influence in the output torque as the material tends to saturate. However, at 0.3 N m, rotor eddy currents increase the torque output by 6.2% (18.6 mN m) with respect to the lossless case.

A final remark is spent to motivate the use of a vector hysteresis model. Figure 5 shows the parametric locus between radial and tangential flux density components in time and at different rotor radial positions. At the rotor inside radius, the magnetic flux density is almost perfectly alternating in the tangential direction: a scalar hysteresis representation would be acceptable. However, in points towards the outside radius, the radial component grows and the tangential one is reduced slightly. At the rotor outside radius, a vector hysteresis model is necessary to reproduce the rotating nature of the field.

The maximum value of $|\mathbf{B}|$ and its time quadrature value can be extracted from the locus in Fig. 5. The ellipticity is simply the percent ratio between the latter term and the former one. In this case, the ellipticity increases from 3.9% at the rotor inside radius up to 89.7% at the outside radius.

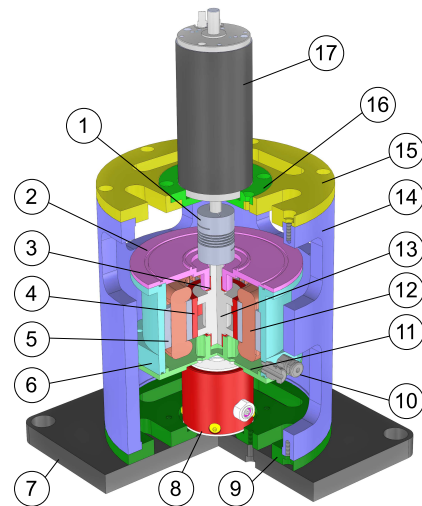


Fig. 6. Test rig mechanical layout. (1) Joint; (2) motor top cover; (3) plastic bushing [$\times 2$]; (4) SHMM rotor ring; (5) stator stack; (6) motor case; (7) rig base; (8) torque meter; (9) rig bottom flange; (10) cable gland [$\times 3$]; (11) motor bottom cover; (12) stator windings; (13) rotor shaft; (14) rig frame; (15) rig top flange; (16) load motor adapter; (17) load motor.

III. EXPERIMENTAL VALIDATION

A. Test Rig

The hysteresis motor prototype was built by following the design guidelines in Section II-C. For experimental validation purposes, a dedicated test rig was also designed and assembled as seen in Fig. 6. In this setup, the prototype is enclosed by a steel frame and coupled to the bottom side of it with a reaction torque meter (Futek model TFF400). On the top side, the motor is connected to a load motor (Maxon RE50 DC motor) by means of a joint. The hysteresis motor prototype is supplied by a three-phase inverter able to impose a sinusoidal current supply at different amplitudes and frequencies. The load motor is fed by a current-controlled H bridge. For monitoring purposes, an incremental optical encoder (Faulhaber HEDL 5540) installed on the load motor is used to measure the speed of both machines during the tests.

The complete experimental setup and the final prototype are shown in Fig. 7. In practice, the hysteresis motor prototype was tested at angular speeds up to 2000 rpm and slot current density amplitudes below 3.9 A/mm². The speed constraint is mainly related to the inability to operate the load motor at higher speeds due to supply voltage limitations. The current density amplitude is bounded to avoid overcoming the torque meter full scale (0.35 N m).

B. Experiments

Due to the working principle of the reaction torque meter, the measurements inevitably miss the mechanical losses in the bearings of the motor that drives the system. Hence, in a preliminary test, the hysteresis motor was mechanically driven by the load motor at different speeds while electrically not supplied to quantify its mechanical losses. In the worst-case, it was found that the torque losses on the bearings are 9.1 mN m at 2500 rpm.

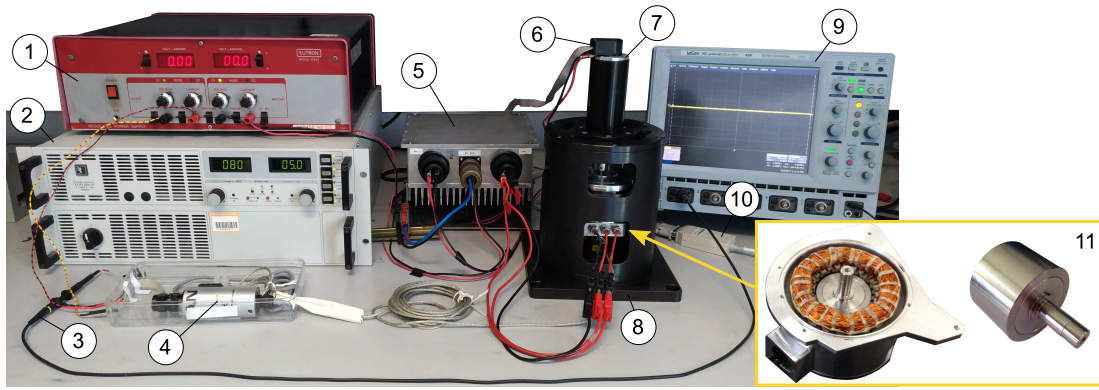


Fig. 7. Experimental setup. (1) Supply for control unit and sensors; (2) supply for power section; (3) voltage probe; (4) torque meter amplifier; (5) control unit for hysteresis and load motors; (6) incremental encoder; (7) load motor; (8) test rig; (9) oscilloscope; (10) CAN interface for PC communication; (11) hysteresis motor prototype.

In a typical run, the hysteresis machine is fed with a sinusoidal three-phase current profile at constant frequency and amplitude. When the prototype reaches the synchronous condition (i.e. $f_m \cong f_s/p$), the load motor is fed to provide a braking torque ramp with a slope of 12 mNm/s. This mechanical load should increase slowly to avoid introducing dynamic contributions to the quasi-static test. For the highest torque measurements, each run can last up to 30 s. When excessive loading is reached, the hysteresis motor becomes unstable and hence, the pull-out torque of the hysteresis motor is measured by registering the output of the torque meter immediately before this instability takes place.

The described run was repeated for all the possible combinations between

- slot current density amplitudes from 1.9 to 3.9 A/mm², step of 0.2 A/mm² and
- rotor speeds from 500 to 2000 rpm with step of 500 rpm.

After each run, it is important to demagnetize the rotor by dragging the hysteresis motor at constant speed while supplying its winding with

$$\begin{cases} J_a = J_s(t) \\ J_b = -J_s(t)/2 \\ J_c = -J_s(t)/2 \end{cases} \quad (18)$$

where $J_s(t)$ is a decreasing current density ramp starting at 3.9 A/mm² and decreasing at a rate of -0.13 A/(s mm²) until the supply is null. This proved to be a valid mechanism to mitigate the effects of previous magnetization on subsequent runs and improve experiment repeatability.

Experimental data are presented in the torque-current density plot in Fig. 8 together with the numerical model output when $\sigma = 0$. The prototype is operating nearby synchronous speed during the experimental characterization. Thus, the eddy currents present on the rotor ring can be mainly attributed to high-order field harmonics. It is expected that they will have a negligible negative impact on the output torque of the machine and the actual torque behavior of the machine will be very close to the ideal case.

Results in Fig. 8 show a close agreement with the proposed model. This outcome is particularly difficult to obtain due to

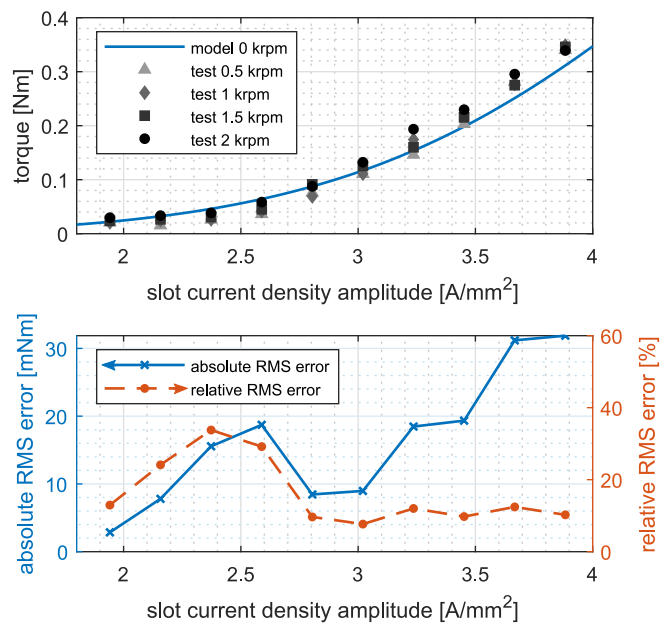


Fig. 8. Numerical versus experimental torque behavior of the hysteresis motor prototype for different slot current density amplitudes. *Top*: Torque data at different speeds are compared to the FE model output ($\sigma = 0$, locked rotor). *Bottom*: The absolute and relative RMS errors between averaged experimental and FE model torque data are also reported.

the highly nonlinear torque characteristic of the hysteresis motor. To give means of comparison, the experimental data were averaged at each current density value and the absolute and relative RMS errors between the model and the experiments were subsequently calculated. A worst-case relative error of 33.8% is obtained at low torque output and absolute error of 15.6 mNm. This condition is critical because the torque meter output signal is particularly sensitive to noise and offsets. Furthermore, variability in the friction torque might induce large relative errors at these measurement levels. In contrast, when the measured output torque is maximum, the absolute error reaches 31.9 mNm, but this value represents only 10.2% of the model output.

In a second test set, the described runs were executed at 2.4, 3.2 and 3.9 A/mm² and 1000 rpm. After each run, the motor

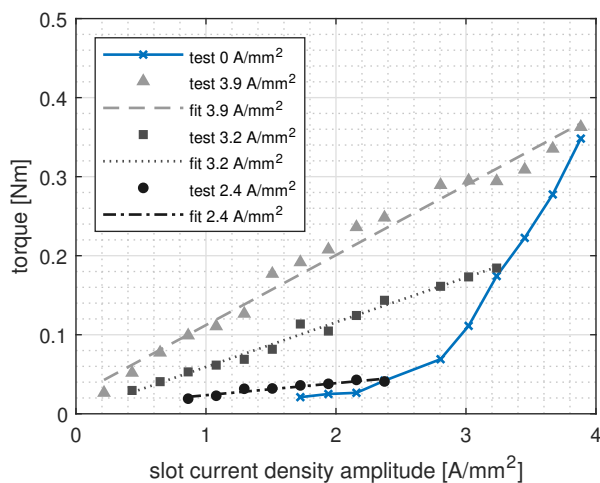


Fig. 9. Experimental torque characteristic obtained at 1000 rpm by feeding the hysteresis motor at 2.4, 3.2 and 3.9 A/mm² and then remeasuring its torque capability at lower current density values. The obtained behavior is fitted with a first degree polynomial. The experimental hysteresis torque without the effects of initial current density excitation is presented as a reference.

was characterized at lower current densities without mitigating the magnetization from the previous test. Results are displayed in Fig. 9. Interestingly, previous magnetization on the rotor has a very positive impact in its performance. In such condition, the motor behaves like a PM synchronous motor, where the torque characteristic and the current (or current density in this case) present a linear relationship. Furthermore, if the initial excitation current density is larger than the value at which the torque is delivered, there is a net gain in the torque capability of the machine with respect to the case where this feature is not exploited. This result encourages the investigation of control strategies able to take into account this property to maximize the output torque of hysteresis machines.

IV. CONCLUSIONS

This paper dealt with the modeling, design and experimental characterization of an inner-rotor hysteresis motor. A time-dependent finite element model was used for the design and numerical assessment of the prototype performance. In this model, the anisotropic SHMM was represented with the vector generalization of the Jiles-Atherton model. The suitability of this numerical tool was proven due to the high nonlinearity of the studied machine and the rotating nature of the magnetic fields within the rotor ring. After a thorough experimental characterization at different speeds and winding electrical loadings, the model demonstrated a close agreement with experimental results. Finally, the prototype was tested following an initial winding overexcitation at different levels. With this technique, the rotor sleeve retains the magnetization achieved during this short supply transient and can potentially behave as a PM synchronous motor when supplied at lower current density values. This feature brings advantages in terms of torque-current linearity and improved torque capability. It encourages further research on hysteresis machines, especially in the high-speed context, where the technology already looks promising.

REFERENCES

- [1] D. Inácio, S. Inácio, J. Pina, A. Gonçalves, M. Ventim Neves and A. Leão Rodrigues, "Numerical and experimental comparison of electromechanical properties and efficiency of HTS and ferromagnetic hysteresis motors," *Journal of Physics: Conference Series*, vol. 97, p. 12218, Feb. 2008.
- [2] A. Canova and F. Cavalli, "Design Procedure for Hysteresis Couplers," *IEEE Trans. Mag.*, vol. 44, no. 10, pp. 2381-2395, Oct. 2008.
- [3] K. R. Rajagopal, "Design of a Compact Hysteresis Motor Used in a Gyroscope," *IEEE Trans. Magn.*, vol. 39, no. 5, pp. 3013-3015, Sep. 2003.
- [4] L. Zhou, M. Imani Nejad, and D. L. Trumper, "One-axis hysteresis motor driven magnetically suspended reaction sphere," *Mechatronics*, vol. 42, pp. 69-80, Apr. 2017.
- [5] R. Galluzzi, A. Tonoli, and N. Amati, "Magnetic hysteresis machines for next-generation electric turbochargers," *2017 International Conference of Electrical and Electronic Technologies for Automotive*, Torino, Italy, pp. 1-5, 2017.
- [6] M. Jagiela, J. Bumby and E. Spooner, "Time-domain and frequency-domain finite element models of a solid-rotor induction/hysteresis motor," *IET Electric Power Applications*, vol. 4, no. 3, pp. 185-197, 2010.
- [7] M. Jagiela, T. Garbiec, and M. Kowol, "Design of High-Speed Hybrid Hysteresis Motor Rotor Using Finite Element Model and Decision Process," *IEEE Trans. Mag.*, vol. 50, no. 2, pp. 861-864, Feb. 2014.
- [8] D. O'Kelly, "Hysteresis motor with overexcitation and solid-state control," *Proc. IEE*, vol. 125, no. 4, pp. 288-292, 1978.
- [9] M. A. Rahman and A. M. Osheiba, "Dynamic Performance Prediction of Polyphase Hysteresis Motors," *IEEE Trans. Ind. Appl.*, vol. 26, no. 6, pp. 1026-1033, Nov./Dec. 1990.
- [10] J. J. Nitao, E. T. Scharlemann and B. A. Kirkendall, *Equivalent Circuit Modeling of Hysteresis Motors*, Lawrence Livermore National Laboratory (LLNL), Livermore, CA, USA, 2009.
- [11] M. Reddy and L. V. Suresh, "Dynamic Analysis Of Hysteresis Motor Using Matlab/Simulink," *International Journal of Engineering Research and Technology*, vol. 1, no. 5, Jul. 2012.
- [12] M. Repetto and P. Uzunov, "Analysis of Hysteresis Motor Starting Torque Using Finite Element Method and Scalar Static Hysteresis Model," *IEEE Trans. Mag.*, vol. 49, no. 5, pp. 2405-2408, May 2013.
- [13] G. Wakui, K. Kurihara, and T. Kubota, "Radial flux type hysteresis motor with reaction torque-Numerical analysis of hysteresis motor using finite element method," *IEEE Trans. Mag.*, vol. 23, no. 5, pp. 3845-3852, Sep. 1987.
- [14] H.-K. Kim, H.-K. Jung, and S.-K. Hong, "Finite element analysis of hysteresis motor using the vector magnetization-dependent model," *IEEE Trans. Mag.*, vol. 34, no. 5, pp. 3495-3498, Sep. 1998.
- [15] M. A. Rahman and A. M. Osheiba, "Improved performance of polyphase hysteresis-reluctance motors fed from single-phase supplies," *IEEE Trans. Ind. Appl.*, vol. 26, no. 1, pp. 130-136, Jan. 1990.
- [16] R. Nasiri-Zarandi and M. Mirsalim, "Finite-Element Analysis of an Axial Flux Hysteresis Motor Based on a Complex Permeability Concept Considering the Saturation of the Hysteresis Loop," *IEEE Trans. Ind. Appl.*, vol. 52, no. 2, pp. 1390-1397, Mar. 2016.
- [17] E. Dlala and A. Arkkio, "Measurement and analysis of hysteresis torque in a high-speed induction machine," *IET Electric Power Applications*, vol. 1, no. 5, pp. 737-742, 2007.
- [18] J. B. Padilha, P. Kuo-Peng, N. Sadowski, and N. J. Batistela, "Vector Hysteresis Model Associated to FEM in a Hysteresis Motor Modeling," *IEEE Trans. Mag.*, vol. 53, no. 6, pp. 1-4, Jun. 2017.
- [19] L. Zhou, W. Gruber, and D. L. Trumper, "Position Control for Hysteresis Motors: Transient-time Model and Field-oriented Control," *IEEE Trans. Ind. Appl.*, vol. 54, no. 4, pp. 3197-3207, Jul. 2018.
- [20] A. J. Bergqvist, "A simple vector generalization of the Jiles-Atherton model of hysteresis," *IEEE Trans. Mag.*, vol. 32, no. 5, pp. 4213-4215, Sep. 1996.
- [21] J. P. A. Bastos and N. Sadowski, *Magnetic Materials and 3D Finite Element Modeling*, Boca Raton, FL, USA: CRC Press, 2016.
- [22] D. G. Dorrell, M.-F. Hsieh, M. Popescu, L. Evans, D. A. Staton, and V. Grout, "A Review of the Design Issues and Techniques for Radial-Flux Brushless Surface and Internal Rare-Earth Permanent-Magnet Motors," *IEEE Trans. Ind. Electron.*, vol. 58, no. 9, pp. 3741-3757, Sep. 2011.
- [23] R. Nasiri-Zarandi, M. Mirsalim, and R. Ashrafi, "Investigation of the effect of winding distribution and slot opening on performance of an axial flux hysteresis motor," *The 6th Power Electronics, Drive Systems & Technologies Conference*, Tehran, Iran, pp. 316-321, 2015.

- [24] A. Arkkio, "Analysis of Induction Motors Based on the Numerical Solution of the Magnetic Field and Circuit Equations," *Acta Polytechnica Scandinavica*, no. 59, Helsinki University of Technology, 1987.
- [25] T. Kubota, G. Wakui, and M. Itagaki, "Hysteresis motor using magnetically anisotropic Fe-Cr-Co magnet," *IEEE Trans. Mag.*, vol. 34, no. 6, pp. 3888-3896, Nov. 1998.
- [26] P. Kis and A. Iványi, "Parameter identification of Jiles-Atherton model with nonlinear least-square method," *Physica B: Condensed Matter*, vol. 343, no. 1-4, pp. 59-64, Jan. 2004.
- [27] I. D. Mayergoyz, *Mathematical Models of Hysteresis and Their Applications*. New York, NY, USA: Elsevier Academic Press, 2003.
- [28] *AC/DC Module User's Guide*, COMSOL 5.3a, 2017.



Andrea Tonoli received his PhD degree (1993) in Machine Design from Politecnico di Torino and joined the faculty in 1994. He is now a full professor in the Mechanical and Aerospace Engineering Department.

He served as Director of the Mechatronics Laboratory of Politecnico di Torino from 2007 to 2011. His research and teaching interests focus on the analysis, design and control of electromechanical systems with an emphasis on: rotating machinery, active and passive magnetic bearings and dampers, piezoelectric transducers for vibration and motion control and electromechanical systems for automotive applications.



Renato Galluzzi received the MSc degree in Mechatronic Engineering from Politecnico di Torino, Italy, in 2010. He joined the Mechatronics Laboratory from the same university in 2011 to later obtain a PhD degree in Mechatronics in 2014. He currently works there as a postdoctoral research fellow.

His research is mainly focused on the integrated design and validation of power actuators, vibration control systems, electric motor drives, magnetic levitation and energy harvesting.



Nicola Amati received the PhD degree in Machine Design from the Department of Mechanical Engineering at Politecnico di Torino, Turin, Italy, in 2001. He joined the faculty of Politecnico di Torino in the same year, where he is now an associate professor in the Mechanical and Aerospace Engineering Department.

His research and teaching interests focus on the analysis, design and control of electromechanical systems with an emphasis on rotating machinery, active and passive magnetic bearings and dampers, and more-electric systems for automotive applications.